One-Pot Synthesis of Trimetallic Au@PdPt Core–Shell Nanoparticles with High Catalytic Performance

Shin Wook Kang, Young Wook Lee, Yangsun Park, Bu-Seo Choi, Jong Wook Hong, Kyu-Hwan Park, and Sang Woo Han*

Department of Chemistry and KI for the NanoCentury, KAIST, Daejeon 305-701, Korea, and Center for Nanomaterials and Chemical Reactions, Institute for Basic Science (IBS), Daejeon 305-701, Korea

ABSTRACT The development of an efficient synthesis method to produce multimetallic nanoparticles (NPs) with a desirable structure is strongly required to clarify the structure–composition–property relationship of NPs and to investigate their possible applications. However, the controlled synthesis of NPs consisting of multiple ($n \geq 3$) noble metal components has been relatively unexplored in comparison to bimetallic NPs. In the present work, we have demonstrated a facile one-pot aqueous approach for the controlled synthesis of trimetallic Au@PdPt core–shell NPs with a well-defined octahedral Au core and a highly crystalline dendritic Pd–Pt alloy shell (Au_{oct}@PdPt NPs). The simultaneous reduction of multiple metal precursors with dual reducing agents, namely, ascorbic acid and hydrazine, gave a fine control over the nucleation and growth kinetics of NPs, resulting in the formation of novel Au_{oct}@PdPt NPs. The prepared NPs showed excellent catalytic performance for methanol electrooxidation, which can be attributed to their optimized binding strength toward adsorbate molecules due to the improved charge transfer between core and shell of the NPs. The present strategy can offer a convenient and valuable way to fabricate multicomponent nanostructures with desired structures and functions.

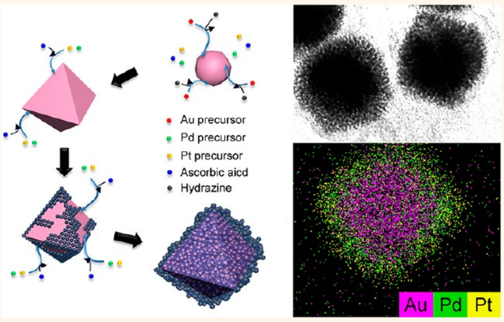

KEYWORDS: core–shell nanoparticles · electrocatalysis · methanol · surface-enhanced Raman scattering · trimetallic

Synthesis of noble metal nanoparticles (NPs) has attracted increasing attention because of their fascinating applications in a variety of fields, such as plasmonics,[1–3] chemical sensing,[4,5] surface-enhanced Raman scattering (SERS),[6–8] drug delivery,[9,10] and catalysis.[11,12] Tremendous effort has been especially devoted to the synthesis of multimetallic NPs due to their advantages, including high selectivity, activity, and chemical/physical stability, in comparison to those of the corresponding monometallic components.[13–16] As in the case of monometallic NPs, the properties of multimetallic NPs are entirely affected by their shape. In particular, NP shape can determine the overall catalytic properties of NPs due to the presence of different types of exposed facets on their surfaces.[17–19] Accordingly, there have been many studies in the past decades on the synthesis of bimetallic NPs with well-defined morphologies, such as octahedral,[20,21] rhombic dodecahedral,[22] prismatic,[23,24] cubic,[25–27] wire-like,[28,29] flower-like,[30,31] and dendritic NPs,[32–34] as well as high-index-faceted NPs,[35–39] for tuning the catalytic activity and selectivity of NPs in various chemical and electrocatalytic reactions.

Despite great advances in this field, the controlled synthesis of NPs consisting of multiple ($n \geq 3$) noble metal components has been relatively unexplored in comparison to bimetallic NPs, although they can provide new insights into the structure–composition–property relationships in noble metal NPs. There have been a few reports on the preparation of trimetallic NPs with well-defined morphologies. For example, Puntes *et al.* reported the preparation of Pd–Au–Ag nanoboxes from Ag nanocubes by sequential or simultaneous galvanic exchange and Kirkendall growth.[40] Yamauchi and co-workers reported the synthesis of spherical Au@Pd@Pt triple-layered core–shell NPs, which have better catalytic activity than bimetallic core–shell NPs.[41,42] Very recently, we succeeded

* Address correspondence to sangwoohan@kaist.ac.kr.

Received for review June 15, 2013 and accepted August 5, 2013.

Published online **August 05, 2013**
10.1021/nn403027j

in the production of Pt–Pd–Ag ternary alloy nanotubes with a nanoporous framework using ZnO nanowires as sacrificial templates.[43] Nevertheless, it is still a highly challenging task to design and synthesize multimetallic NPs with well-defined morphologies due to the formidable difficulties in controlling the nucleation/growth kinetics of NPs in the presence of multiple metal precursors with different reduction potentials. As such, preformed NP seeds or structure-directing templates have been commonly employed to generate nanostructures with multiple metallic constituents. Therefore, the development of an efficient and straightforward synthetic route to prepare multimetallic NPs with a desirable structure is quite demanding to determine their characteristics and investigate their possible applications.

We demonstrate here that trimetallic Au@PdPt core–shell NPs with a well-defined octahedral Au core and a dendritic Pd–Pt alloy shell (Au_{oct}@PdPt NPs) can be synthesized in a high yield by a facile aqueous one-pot synthesis method with no assistance of a presynthesized seed or template. The co-reduction of multiple metal precursors with dual reducing agents (ascorbic acid and hydrazine) gave a fine control over the nucleation and growth kinetics of NPs, resulting in the formation of Au_{oct}@PdPt NPs. Since the present one-pot method does not require multiple steps, such as seed preparation and an intermediate workup process, the synthesis of multimetallic NPs with a well-defined shape could be greatly simplified. Furthermore, the prepared NPs showed excellent catalytic activity and stability for the electrooxidation of methanol in acidic media.

RESULTS AND DISCUSSION

In a typical synthesis of Au_{oct}@PdPt NPs, a $HAuCl_4$/K_2PdCl_4/K_2PtCl_6 mixture in a molar ratio of 1:1:1 was simultaneously reduced by both ascorbic acid and hydrazine in the presence of cetyltrimethylammonium chloride (CTAC) (see the Method section for details). Figure 1a and b show representative scanning electron microscopy (SEM) and transmission electron microscopy (TEM) images of the as-synthesized Au_{oct}@PdPt core–shell NPs, respectively, demonstrating the high-yield (>90%) production of NPs. The high-angle annular dark-field scanning TEM (HAADF-STEM) and high-resolution TEM (HRTEM) images of a NP clearly show that NPs have an octahedral shape overall, which consists of an octahedral core and a uniform dendritic shell (inset of Figure 1b and c). The average edge length of the Au_{oct}@PdPt NPs measured by TEM images was 61.0 ± 1.3 nm. The average edge length of the core and the shell thickness were 38.3 ± 3.8 and 13.6 ± 1.6 nm, respectively. The high-magnification HRTEM image (Figure 1d) and corresponding selected

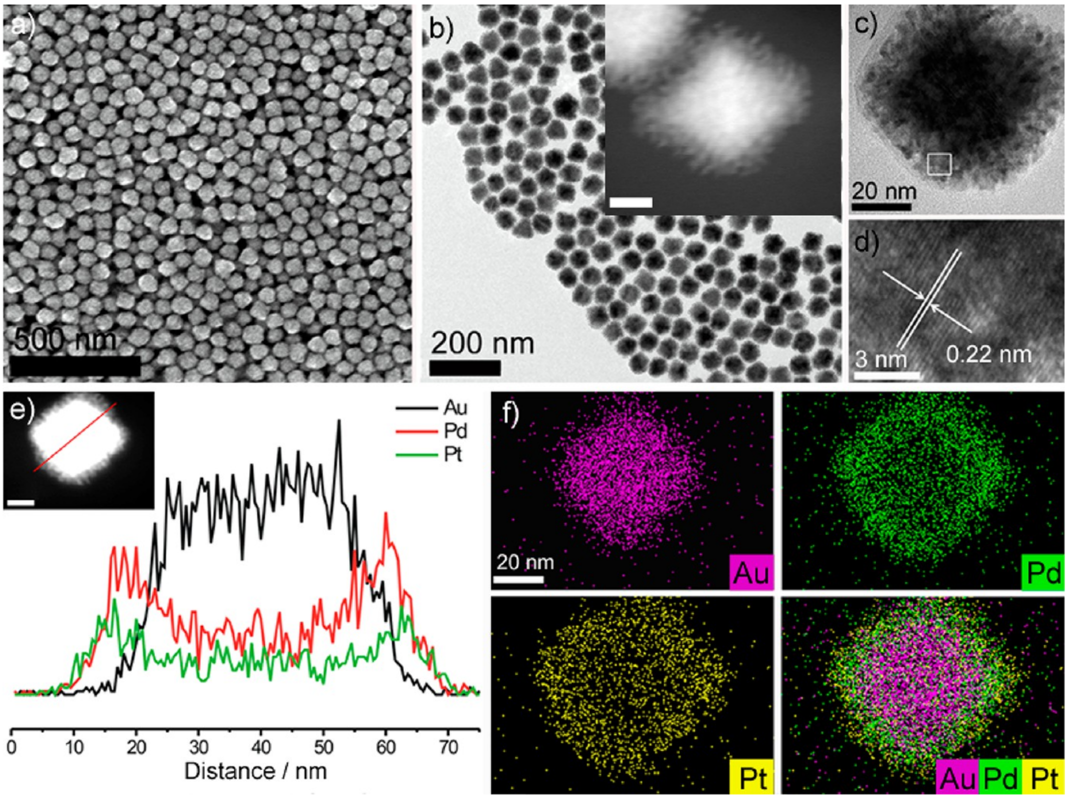

Figure 1. (a) SEM, (b) TEM, and (c) HRTEM images of the Au_{oct}@PdPt NPs. HAADF-STEM image of a NP is shown in the inset of (b). Scale bar indicates 20 nm. (d) High-magnification HRTEM image of the square region in (c). (e) HAADF-STEM image and cross-sectional compositional line profiles of an Au_{oct}@PdPt NP. Scale bar indicates 20 nm. (f) HAADF-STEM-EDS elemental mapping images of an Au_{oct}@PdPt NP.

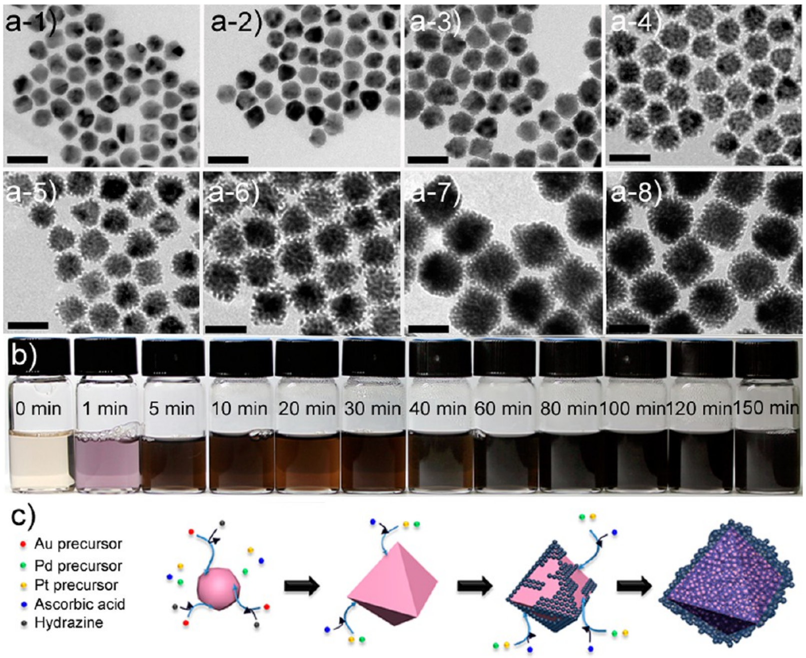

Figure 2. TEM images of NPs collected at different reaction times: (a-1) 1, (a-2) 10, (a-3) 20, (a-4) 40, (a-5) 60, (a-6) 100, (a-7) 120, and (a-8) 150 min. Scale bars indicate 50 nm. (b) Photographs of reaction solution reacted under different reaction times. (c) Schematic illustration of the formation mechanism of the Au_{oct}@PdPt NPs.

area electron diffraction (SAED) pattern of the square region in Figure 1c (Figure S1a in the Supporting Information (SI)) demonstrate the single crystallinity of the Pd–Pt shell in the prepared NPs. The *d*-spacing of 0.22 nm for adjacent lattice fringes matches well with that of the (111) planes of face-centered cubic (fcc) Pd–Pt alloy,[44,45] indicating that the exposed facets of the Pd–Pt shell in the Au_{oct}@PdPt NPs are mostly {111}. HAADF-STEM–energy-dispersive X-ray spectroscopy (EDS) measurements were performed to get more insight into the distribution of each element in the NPs. As shown in Figure 1e, the cross-sectional compositional line profiles reveal the presence of a Au core and a Pd–Pt alloy shell in the Au_{oct}@PdPt NPs. EDS elemental mapping images further confirm the core–shell structure of the Au_{oct}@PdPt NPs (Figure 1f). The X-ray diffraction (XRD) pattern of the Au_{oct}@PdPt NPs also reveals their core–shell structures (Figure S2a in SI). Typical diffraction peaks, which could be indexed to the reflections of fcc structure of metal, were observed. Notably, peak positions are similar to those of pure Au. However, each XRD peak has an asymmetric line shape inclined toward the higher-angle side. This can be attributed to the Pd–Pt shell, in line with previous observations for other bimetallic core–shell NPs.[36,46] The Au:Pd:Pt atomic ratio of the Au_{oct}@PdPt NPs was estimated to be 55:25:20 by inductively coupled plasma atomic emission spectroscopy (ICP-AES).

The morphological evolution of the NPs was investigated by measurement of the TEM images of NPs sampled at different reaction times (Figure 2a). Octahedral NPs with an average edge length of 30.3 ± 2.0 nm were initially formed in 1 min (Figure 2a-1). After 10 min of reaction, small protrusions started to grow over the surface of the NPs (Figure 2a-2), and numerous branches were clearly visible after 20 min (Figure 2a-3). These dendritic branches grew further as the reaction time increased (Figures 2a-4–7), and eventually, well-defined Au_{oct}@PdPt core–shell NPs were produced in 150 min (Figure 2a-8). The shape evolution of the NPs was also reflected in the color change of the reaction solution (Figure 2b). The color of the solution changed from turbid yellow to pink, dark brown, and finally to black over the course of reaction, which corresponds to the sequential formation of Au NP cores and Au_{oct}@PdPt core–shell NPs (Figure 2c). The change in composition of each metal element and the variation of NP size during the reaction estimated by ICP-AES and TEM analyses, respectively, further confirmed that Au precursors were initially reduced to form Au NP cores, followed by the deposition of Pd and Pt onto the formed Au cores (Figure 3).

The formation of Au_{oct}@PdPt core–shell NPs could be the result of controlled nucleation/growth kinetics of NPs, which was manipulated by the reducing agents used in the synthesis, *i.e.*, ascorbic acid and hydrazine. To decipher the formation mechanism of the Au_{oct}@PdPt NPs, several control experiments were performed. In a previous work, we showed that Au@Pd core–shell nanocrystals with {111}-faceted octahedral structure were formed when $AuCl_4^-$ and $PdCl_4^-$ precursors were co-reduced by CTAC at ~90 °C in an oven for 48 h in the absence of additional reducing agent.[46] On the basis of this fact, the growth of octahedral

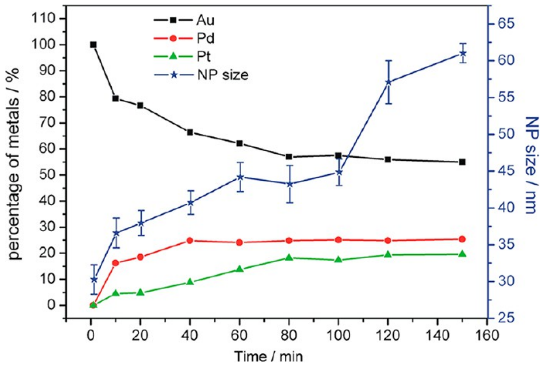

Figure 3. Compositional changes for each metal element and the variation of NP size during the reaction estimated by ICP-AES and TEM analyses, respectively.

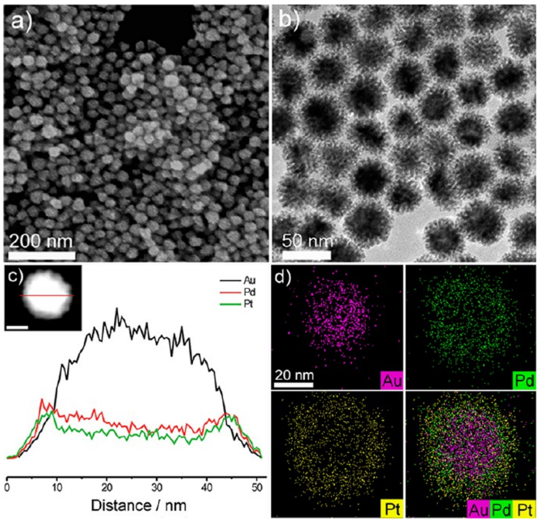

Figure 4. (a) SEM and (b) TEM images of the Au$_{\text{sph}}$@PdPt NPs. (c) HAADF-STEM image and cross-sectional compositional line profiles of an Au$_{\text{sph}}$@PdPt NP. Scale bar indicates 20 nm. (d) HAADF-STEM-EDS elemental mapping images of the Au$_{\text{sph}}$@PdPt NP.

Au@Pd−Pt core−shell nanocrystals is expected when Pt precursor is added in this system. However, as shown in Figure 4, dendritic Au@PdPt NPs with spherical shape overall (Au$_{\text{sph}}$@PdPt NPs) were formed when the mixture of HAuCl$_4$/K$_2$PdCl$_4$/K$_2$PtCl$_6$ in a molar ratio of 1:1:1 was co-reduced with CTAC without any additional reductants, such as ascorbic acid and hydrazine, at 95 °C in an oven for 48 h. SEM and TEM images of the products showed that Au$_{\text{sph}}$@PdPt NPs have a spherical structure with an average size of 43.3 ± 5.1 nm (Figure 4a and b). The average core diameter and shell thickness were 27.8 ± 3.9 and 7.6 ± 1.3 nm, respectively. HAADF-STEM, EDS, and XRD measurements revealed the core−shell structure of the NPs (Figure 4c and d, Figure S2b in SI), consisting of a spherical Au core and a dendritic Pd−Pt alloy shell. The Au:Pd:Pt atomic ratio of the Au$_{\text{sph}}$@PdPt NPs was determined to be 41:32:27 by ICP-AES. Notably, in contrast to the case of Au$_{\text{oct}}$@PdPt NPs, the SAED pattern obtained from the shell of Au$_{\text{sph}}$@PdPt NPs indicated the polycrystalline nature of the Pd−Pt shell (Figure S1b in SI), implying that the structure of the Au NP core can determine the crystallinity of the Pd−Pt shell grown on its surface.[47] From these observations, it can be inferred that the existence of a Pt precursor might affect the NP growth habit by interacting with a surfactant and/or other metal precursors (*vide infra*). In fact, the presence of multiple metal precursors in the reaction media induces complicated reduction kinetics as a result of mutual interaction as well as complexation with surfactant molecules and reductants.[48−50] The successful generation of the Au$_{\text{oct}}$@PdPt core−shell NPs with well-defined octahedral Au core and dendritic Pd−Pt shell was achieved exclusively when both ascorbic acid and hydrazine were employed in the synthesis as reducing agents. When ascorbic acid was solely used as a reductant in the synthesis, dendritic Pd−Pt alloy NPs were produced instead of ternary Au−Pd−Pt NPs (Figure S3a and b in SI). Elemental mapping of Pd and Pt on the prepared NPs (Figure S3c in SI) and compositional line profiles on an individual NP (Figure S3d in SI) obtained by HAADF-STEM-EDS reveal that the synthesized NPs were definitely a Pd−Pt alloy. The Pd:Pt atomic ratio of the dendritic Pd−Pt alloy NPs was estimated to be 65:35 by ICP-AES. Surprisingly, despite the higher reduction potential of an Au precursor than Pd and Pt ones (the standard reduction potentials of Au(III) (AuCl$_4^-$/Au), Pd(II) (PdCl$_4^{2-}$/Pd), and Pt(IV) (PtCl$_6^{2-}$/Pt) are +1.498, +0.591, and +0.68 V *vs* SHE (standard hydrogen electrode), respectively),[51,52] Au was not detected in the elemental analysis of NPs with EDS (Figure S3e in SI) and ICP-AES. As previously mentioned, the nucleation and growth mechanism of NPs in the presence of multiple metal precursors and surfactant molecules cannot be explained simply in terms of the reduction potentials of the metal precursors due to their complicated reduction kinetics. On the other hand, polyhedral Au NPs with a variety of shapes were produced when mixed metal precursors were reduced only by hydrazine, while the other experimental conditions were kept unchanged (Figure S4a and b in SI). Noticeably, the EDS elemental analysis for the prepared NPs showed no signal of Pd or Pt (Figure S4c in SI). These findings unambiguously demonstrate that the use of dual reductants is indispensable for the successful formation of trimetallic Au$_{\text{oct}}$@PdPt core−shell NPs under our experimental conditions: hydrazine and ascorbic acid facilitate, respectively, the generation of the Au core and dendritic Pd−Pt shell of NPs.

Regarding the formation mechanism of the Au$_{\text{oct}}$@PdPt NPs, a remaining issue is the origin of the formation of octahedral Au NP cores. In this regard, it is worth pointing out that homogeneous Au NPs with an octahedral shape (average edge length = 45.8 ± 3.8 nm) were produced when a HAuCl$_4$/K$_2$PdCl$_4$ mixture was

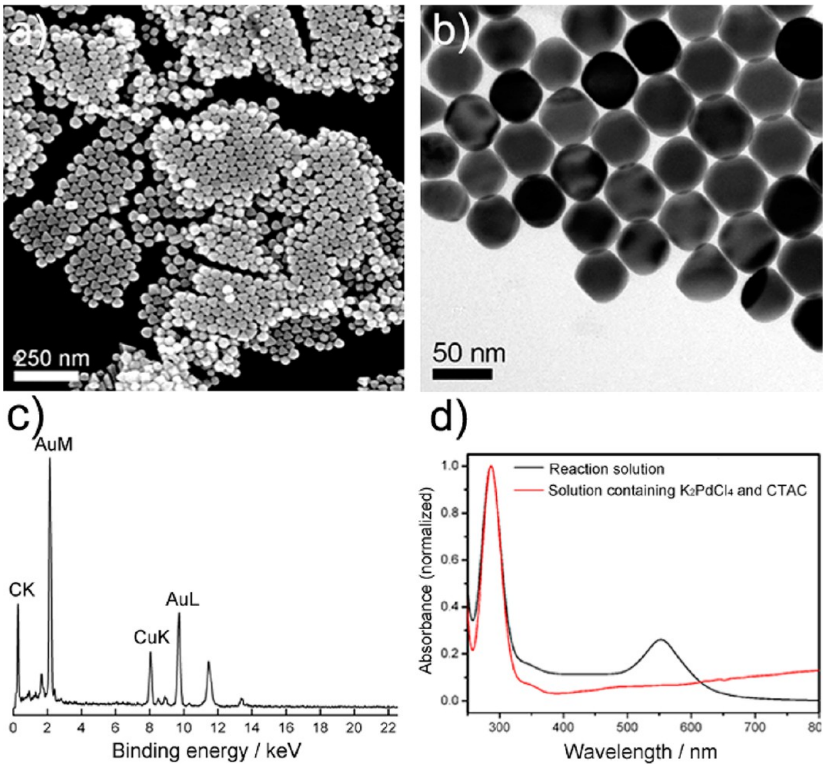

Figure 5. (a) SEM and (b) TEM images of NPs prepared by reducing the $HAuCl_4/K_2PdCl_4$ mixture by hydrazine. (c) EDS spectrum of the prepared NPs. (d) UV−vis absorption spectra of the reaction solution (black curve) and an aqueous solution containing Pd precursor and CTAC (red curve).

reduced by hydrazine (Figure 5a and b), whereas the reduction of a $HAuCl_4/K_2PdCl_4/K_2PtCl_6$ mixture by hydrazine yielded polyhedral Au NPs of various shapes (Figure S4 in SI). The EDS analysis of the purified NPs showed no signal of Pd (Figure 5c). The UV−vis absorption spectrum of the reaction solution showed an absorption peak at 553 nm, which can be assigned to the dipole surface plasmon resonance (SPR) mode of octahedral Au NPs (Figure 5d).[53] Interestingly, an additional strong absorption peak was also identified at 285 nm in the UV−vis spectrum. From the comparison with the UV−vis absorption spectrum of an aqueous solution containing Pd precursor and CTAC, this peak can be assigned to the ligand-to-metal charge transfer (LMCT) peak of a complex formed between Pd precursor and CTAC molecules.[54] These experimental results explicitly indicate that the Pd precursor−CTAC complex plays a crucial role in the formation of Au NPs with the well-defined octahedral shape. In fact, it has been reported that Pd precursor−surfactant molecule complexes manipulate the nucleation and growth of NPs, thus providing fine control over the final morphology of products.[35,55−57] When other non-ammonium surfactants, such as sodium dodecyl sulfate (SDS), F127, P123, and Brij58, were used instead of CTAC, NPs of various shapes with nonuniform size were produced (Figure S5 in SI). The production of inhomogeneous Au NPs with hydrazine in the presence of Pt precursors can then be ascribed to the inhibition of complex formation between the Pd precursor and the surfactant molecules by the Pt precursor due to its stronger binding affinity to N-containing surfactant molecules than Pd precursor.[58,59] On the basis of these observations and findings together with the fact that the Au_{oct}@PdPt NPs with well-defined octahedral Au NP cores were formed when both ascorbic acid and hydrazine were used, we can infer that ascorbic acid not only facilitates the deposition of a Pd−Pt shell on a Au core but also effectively prohibits the aforementioned inhibition action of Pt precursor, thus promoting the structure-directing activity of the Pd precursor−CTAC complex toward the formation of an octahedral Au core. Taken together, we can identify the formation mechanism of the Au_{oct}@PdPt NPs (Figure 2c). At the initial stage of reaction, Au precursors are reduced by hydrazine to form octahedral Au NP cores with the assistance of the Pd precursor−CTAC complex as a structure-regulating agent. Subsequently, Pd−Pt alloy shells are grown on the surface of the Au cores by ascorbic acid.

A series of control experiments with different ratios of metal precursors and reducing agents compared to the standard synthesis conditions validated further the proposed mechanism and the importance of growth kinetic control for the formation of Au_{oct}@PdPt NPs. For instance, reactions with 2:1:1 and 1:1:2 molar ratios of a $HAuCl_4/K_2PdCl_4/K_2PtCl_6$ mixture did not yield well-defined Au_{oct}@PdPt NPs (Figure S6a and b in SI);

instead, irregularly shaped NPs with a broad size distribution were produced. It can be inferred that the relative concentration of Pd precursor is not enough to direct the formation of homogeneous Au NP cores with octahedral shape in the case of the 2:1:1 molar ratio of mixed metal precursors, and ascorbic acid cannot fully prohibit the inhibition action of Pt precursor in the case of the 1:1:2 ratio of mixed metal precursors due to the high relative concentration of Pt precursor. In contrast, when a metal precursor mixture with 1:2:1 molar ratio was used, uniform-sized Au@PdPt NPs were generated (Figure S6c in SI). However, the shape of the Au core could not be regulated (Figure S6d in SI), indicating that the excess amount of Pd precursor cannot effectively drive the formation of uniform octahedral Au NP cores. These results reveal that the proper Au/Pd/Pt ratio in the precursor solution can generate well-defined $\mathrm{Au_{oct}}$@PdPt NPs through fine control over the nucleation/growth kinetics of Au cores. In addition, the relative concentration of hydrazine and ascorbic acid was also crucial for the formation of the $\mathrm{Au_{oct}}$@PdPt NPs. When the concentration of hydrazine was decreased by half, while the other conditions were retained, large core–shell NPs with no particular shape were produced (Figure S7a in SI). This implies that the concentration of hydrazine was not sufficient to produce the appropriate amount of Au NP cores with octahedral shape. On the contrary, $\mathrm{Au_{oct}}$@PdPt NPs were obtained by increasing the concentration of hydrazine by 2-fold; however, the yield was less than 50% (Figure S7b in SI). On the other hand, decreasing the concentration of ascorbic acid by half under otherwise identical experimental conditions to the standard procedure did not lead to the formation of $\mathrm{Au_{oct}}$@PdPt NPs (Figure S7c in SI). This can be ascribed to the fact that the low concentration of ascorbic acid cannot effectively block the inhibition action of Pt precursor, as in the case of reaction with a 1:1:2 molar ratio of a $\mathrm{HAuCl_4/K_2PdCl_4/K_2PtCl_6}$ mixture (Figure S6b in SI). Meanwhile, the low-yield (~50%) production of $\mathrm{Au_{oct}}$@PdPt NPs with somewhat thick Pd–Pt shells was observed when the concentration of ascorbic acid was increased by 2-fold (Figure S7d in SI). These findings collectively verify the formation mechanism of the $\mathrm{Au_{oct}}$@PdPt NPs and distinctly demonstrate that maneuvering the NP growth kinetics by employing the proper amount of metal precursors and reductants is the key to controlling the final morphology of NPs.

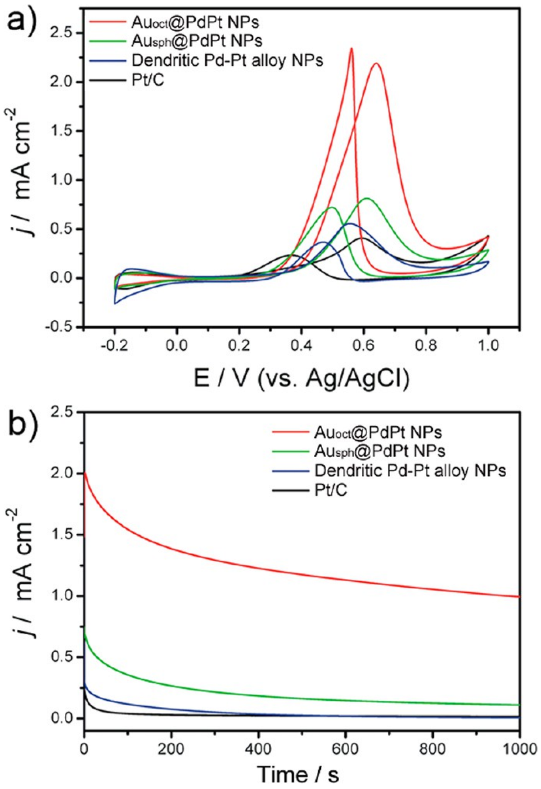

Figure 6. (a) CVs in 0.1 M $\mathrm{HClO_4}$ + 0.5 M methanol of $\mathrm{Au_{oct}}$@PdPt NPs, $\mathrm{Au_{sph}}$@PdPt NPs, dendritic Pd–Pt alloy NPs, and Pt/C catalysts. Scan rate = 50 mV $\mathrm{s^{-1}}$. (b) CA curves for the various catalysts in 0.1 M $\mathrm{HClO_4}$ + 0.5 M methanol at 0.6 V *vs* Ag/AgCl.

The electrocatalytic activity of the $\mathrm{Au_{oct}}$@PdPt NPs toward methanol oxidation was tested to investigate the catalytic performance of the prepared NPs, and the results were compared with those of the $\mathrm{Au_{sph}}$@PdPt NPs (Figure 4), dendritic Pd–Pt alloy NPs (Figure S3 in SI), and a commercial Pt/C catalyst (Johnson Matthey, 20 wt %, average Pt particle size = 3 nm, see Figure S8 in SI). The surface compositions of the $\mathrm{Au_{oct}}$@PdPt, $\mathrm{Au_{sph}}$@PdPt, and dendritic Pd–Pt NPs were determined to be Pd:Pt = 49:51, 50:50, and 48:52, respectively, by X-ray photoelectron spectroscopy (XPS), indicating that these NPs had similar surface compositions. Figure 6a shows the cyclic voltammograms (CVs) of methanol oxidation obtained with different catalysts, in which characteristic methanol oxidation peaks are identified in the forward and backward sweeps. The currents were normalized to the electrochemically active surface area (ECSA) of each catalyst, which was calculated by measurement of the Coulombic charge for hydrogen underpotential desorption in the CVs of catalysts in 0.1 M $\mathrm{HClO_4}$ (Table 1 and Figure S9 in SI). It is apparent that the catalytic activity of the $\mathrm{Au_{oct}}$@PdPt NPs is significantly higher than those of other catalysts: the peak current density of the $\mathrm{Au_{oct}}$@PdPt NPs is 2.7, 3.9, and 5.2 times higher than those of the $\mathrm{Au_{sph}}$@PdPt NPs, dendritic Pd–Pt alloy NPs, and Pt/C, respectively (Table 1). Furthermore, the $\mathrm{Au_{oct}}$@PdPt NPs exhibited a greatly improved mass activity compared to those of other catalysts (Table 1). It is worth mentioning that a large difference in catalytic performance was observed between the $\mathrm{Au_{oct}}$@PdPt and $\mathrm{Au_{sph}}$@PdPt NPs, although both NPs had Au@PdPt core–shell structures consisting of a Au NP core and a dendritic Pd–Pt alloy shell, and they showed similar ECSA values and surface compositions. This demonstrates that the shape of the Au core has a profound effect on the catalytic activity of NPs. Furthermore, the

TABLE 1. ECSA and Catalytic Properties toward Methanol Oxidation for Each Catalyst

catalyst	ECSA ($m^2\ g^{-1}$)	current density ($mA\ cm^{-2}$)	mass activity ($mA\ mg_{Pt}^{-1}$)
Au_{oct}@PdPt NPs	69.3 ± 2.2	2.19 ± 0.04	1485 ± 26
Au_{sph}@PdPt NPs	67.6 ± 6.9	0.802 ± 0.039	504.5 ± 24.6
dendritic Pd−Pt alloy NPs	16.7 ± 1.8	0.566 ± 0.015	102.1 ± 2.7
Pt/C	34.3 ± 0.4	0.403 ± 0.022	149.3 ± 8.1

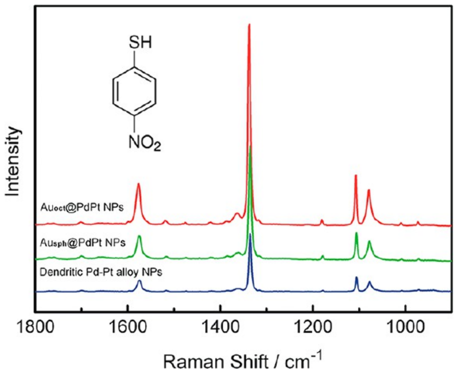

Figure 7. SERS spectra of 4-NBT obtained with the Au_{oct}@PdPt, Au_{sph}@PdPt, and dendritic Pd−Pt alloy NPs.

chronoamperometry (CA) curve for the Au_{oct}@PdPt NPs exhibited a slower current attenuation with much high retention of current after 1000 s compared to other catalysts (Figure 6b), revealing that the octahedral Au core of the Au_{oct}@PdPt NPs could promote catalytic stability as well as activity in the electrooxidation of methanol.

A comparison of the catalytic activity of different catalysts explicitly indicates that the pronounced electrocatalytic activity of the Au_{oct}@PdPt NPs can be attributed to the presence of the well-defined octahedral Au NP core and the Pd−Pt alloy shell of the NPs. The electrocatalysis experiments showed that the catalysts consisting of bimetallic Pd−Pt alloy surfaces have higher specific activities for methanol electrooxidation than the Pt/C catalyst. It is widely known that the catalytic function of Pt can be enhanced by alloying with Pd due to the synergism between Pt and Pd.[60,61] In addition, the presence of a high-index stepped surface in the dendritic Au@PdPt and Pd−Pt NPs might also contribute to their enhanced catalytic function.[62] On the other hand, the higher catalytic activities of Au@PdPt catalysts compared to that of dendritic Pd−Pt alloy NPs can be ascribed to the promoted electronic structure modification of Pt by the Au cores. In core−shell NP catalysts, the modification of the electronic structure of the shell metal through a charge transfer between core and shell elements plays a decisive role in determining the catalytic activity of NPs, as it can tune the binding energy of reaction intermediates on the NP surfaces.[63−66] For instance, Nørskov *et al*. reported that the rate of reaction catalyzed by core−shell NPs increases as the d-band center of the shell metal is shifted more negatively with respect to the Fermi level due to the decreased adsorption strength of intermediates.[67−69] In fact, XPS measurements on the Pt 4f core level of the different catalysts revealed that the Pt 4f binding energies of the Au@PdPt NPs were blue-shifted compared to that of the dendritic Pd−Pt alloy NPs (Figure S10 in SI). Considering the high correlation between core level and valence band XPS measurements,[70,71] this indicates that the d-band centers of the Au@PdPt NP catalysts shifted downward compared to that of the dendritic Pd−Pt alloy NP catalyst. Therefore, the enhanced electrocatalytic activities of the Au@PdPt NP catalysts can be attributed to their optimized binding affinity for adsorbates compared to the Pd−Pt alloy NP catalyst. More interestingly, the Au_{oct}@PdPt NPs had more positive Pt 4f binding energy than the Au_{sph}@PdPt NPs, which was in good accordance with the electrocatalysis results. This reveals that the charge transfer between the Au core and the Pd−Pt shell could be more facilitated in the Au_{oct}@PdPt NPs compared to the Au_{sph}@PdPt NPs, resulting in their highly pronounced electrocatalytic activity. The enhanced charge transfer in the Au_{oct}@PdPt NPs might be due to their inherent structural characteristics. The well-defined octahedral Au core and the highly crystalline Pd−Pt alloy shell of the NPs can ensure the formation of a core/shell interface with very few defects. Recently, a similar core morphology-dependent electrical property of core−shell NPs was reported by Huang *et al*., where Au−Cu_2O core−shell NPs with an octahedral shape were more conductive than those with a cubic morphology because an octahedral Au NP core could provide a conduction pathway to enhance the conductivity of core−shell NPs.[72] This together with our findings indicates that the shape of the inner core of core−shell NPs should exert a significant effect on the charge transfer characteristics of NPs.

In order to gain more insight into the improved charge transfer in the Au_{oct}@PdPt NP system, we investigated the surface-enhanced Raman scattering properties of the prepared NPs. Figure 7 shows the SERS spectra of 4-nitrobenzenethiol (4-NBT) obtained with the Au_{oct}@PdPt NPs, Au_{sph}@PdPt NPs, and dendritic Pd−Pt alloy NPs. Prominent SERS peaks at 1336 cm^{-1} associated with the symmetric stretching vibration of the nitro group ($\nu_s(NO_2)$) show that the nitro group was not changed upon the adsorption of 4-NBT on the NP surfaces.[73] Interestingly, the SERS intensity of 4-NBT on the Au_{oct}@PdPt NPs was about 2 and 4 times higher than those on the Au_{sph}@PdPt NPs and dendritic Pd−Pt alloy NPs, respectively. The enhanced SERS signals from the Au_{oct}@PdPt and Au_{sph}@PdPt NPs compared to the Pd−Pt NPs can be attributed to the long-range effect of the strong electromagnetic field generated by the plasmonic Au cores of the NPs.[74,75] In fact, the UV−vis extinction spectra of the Au_{oct}@PdPt and Au_{sph}@PdPt NPs in water exhibited broad SPR peaks in the range 500−600 nm, which can be attributed to the dipole plasmon resonance of the Au core (Figure S11 in SI). The SPR peaks of the Au@PdPt NPs were broadened and decreased in intensity compared to that of bare Au NPs (Figure 5d) due to the damping of the dipolar plasmon oscillations of the Au cores by the Pd−Pt shells.[76,77] Notably, despite the similar SPR absorption features of both Au@PdPt NPs, the Au_{oct}@PdPt NPs showed a 2-fold increase in SERS intensity as compared to the Au_{sph}@PdPt NPs. The cause of this enhanced SERS activity of the Au_{oct}@PdPt NPs may be the facilitation of the charge transfer in the NPs. Although the enhancement of the localized electromagnetic field due to the SPR is indeed the main contribution for SERS on metal nanostructures (the electromagnetic enhancement mechanism), the charge transfer between metal and adsorbate molecules can also contribute to the SERS effect of nanostructures to some extent because it is a resonance Raman-like process (the chemical enhancement mechanism).[78−80] The results of SERS measurements thus revealed the improved charge transfer in the Au_{oct}@PdPt NP system, which was in good agreement with the electrocatalysis and XPS results. Further experimental and theoretical studies on the catalytic properties and charge transfer kinetics of the Au_{oct}@PdPt NPs are required to clarify the enhanced catalytic function of the NPs, and such studies are ongoing in our laboratory.

CONCLUSION

We have developed a facile one-pot aqueous synthesis method for the production of trimetallic Au@PdPt core−shell NPs with a well-defined octahedral Au core and a highly crystalline Pd−Pt alloy shell. The successful synthesis of Au_{oct}@PdPt NPs was accomplished by control over the nucleation and growth kinetics of NPs, which was manipulated by the reducing agents used in the synthesis. The prepared NPs showed excellent electrocatalytic performance toward methanol oxidation as compared to other catalysts. The enhanced catalytic function of the Au_{oct}@PdPt NPs can be attributed to their optimized binding affinity for adsorbates due to the improved charge transfer between the core and shell of the NPs. The facilitated charge transfer in the Au_{oct}@PdPt NPs originates from their well-defined structural characteristics, revealing the importance of core structure in the application of core−shell NPs. We expect that the present work will be extended to the synthesis of other multicomponent nanostructures with desired functions, and further improvement of catalytic function and its application to other valuable chemical reactions are expected through precise tuning of the structure and composition of NPs. Furthermore, given the prominent catalytic activity as well as the distinct SERS efficiency of the Au_{oct}@PdPt NPs, label-free *in situ* SERS monitoring of catalytic reactions can be realized using the presented core−shell nanostructure.[81,82]

METHODS

Chemicals and Materials. $HAuCl_4$ (Aldrich, 99.99+%), K_2PdCl_4 (Aldrich, 98%), K_2PtCl_6 (Aldrich, 98%), ascorbic acid (Dae Jung Chemicals & Metals Co., 99.5%), CTAC (Aldrich, solution in water, 25 wt %), hydrazine hydrate ($N_2H_4 \cdot H_2O$, Aldrich, 64%), Pt/C (Johnson Matthey, 20 wt %), and 4-NBT (TCI, >90%) were all used as received. Milli-Q water with a resistivity of greater than 18.0 MΩ·cm was used in the preparation of aqueous solutions.

Synthesis of the Au_{oct}@PdPt NPs. In a typical synthesis of Au_{oct}@PdPt NPs, 1 mL of a 5 mM aqueous solution of a $HAuCl_4/K_2PdCl_4/K_2PtCl_6$ mixture in a molar ratio of 1:1:1 was added into 5 mL of a 100 mM aqueous solution of CTAC. To this solution was added an aqueous solution of ascorbic acid (100 mM, 50 μL), and the mixture was shaken gently. Then, 50 μL of a 16.81 mM aqueous solution of hydrazine was added, and the resultant solution was sealed, heated to 95 °C in a conventional forced-convection oven, and maintained at that temperature for 150 min. The resultant hydrosol was subjected to centrifugation (11 000 rpm for 5 min 30 s, three times) to remove excess reagents.

Characterization of NPs. SEM images of the samples were taken with a field-emission scanning electron microscope (FESEM, FEI model Nova230). TEM images of EDS data were obtained with a JEOL JEM-2010 transmission electron microscope operating at 200 kV after placing a drop of hydrosol on carbon-coated Cu grids (200 mesh). HRTEM, HAADF-STEM, and SAED measurements were performed with a FEI Tecnai G2 F30 Super-Twin transmission electron microscope operating at 300 kV. XRD patterns were obtained with a Bruker AXS D8 DISCOVER diffractometer using Cu Kα (0.1542 nm) radiation. The composition of products was determined by ICP-AES (OPTIMA 3300DV). XPS measurements were carried out using a Thermo VG Scientific Sigma Probe spectrometer with Al Kα X-ray (1486.6 eV) as the light source. XPS data were calibrated using the C 1s peak at 284.6 eV.

Electrochemical Measurements. CV and CA measurements were carried out in a conventional three-electrode cell using a CH Instruments model 600C potentiostat. The working electrodes were fabricated by dropping electrocatalysts onto glassy carbon electrodes (GCEs) with a diameter of 3 mm. Pt wire and Ag/AgCl (in saturated NaCl) were used as the counter and reference electrodes, respectively. Prior to catalyst loading, the GCEs were polished with alumina powder and washed thoroughly with Milli-Q water. The amount of electrocatalysts loaded onto the GCE was adjusted to 14.08 μg_{Pt} cm^{-2} based on the ICP-AES data. The electrocatalysts-modified GCEs were covered with 0.05% Nafion solution and dried at room temperature. The dried GCEs were cleaned again by washing with water and then electrochemically cleaned by 25 potential cycles at a scan rate of 50 mV s^{-1} between −0.20 and 1.00 V *vs* Ag/AgCl in 0.1 M $HClO_4$ to remove residual stabilizing agents on the catalyst surfaces. All CVs were obtained at room temperature. The electrolyte solutions were purged with high-purity N_2 gas before use for about 1 h. The ECSA was estimated by the following equation: ECSA = Q_o/q_o, where Q_o is the surface charge that can be obtained from the area under the CV trace of hydrogen desorption (see Figure S6 in SI) and q_o is the charge required for desorption of a monolayer of hydrogen on the Pd−Pt (Au@PdPt and dendritic Pd−Pt NPs) or Pt surface (Pt/C) (211 or 210 $\mu C/cm^2$ for Pd−Pt or Pt surface, respectively).[83]

SERS Measurements. For SERS measurements, drop-cast films of NPs on a Si substrate were soaked in 0.1 mM 4-NBT solution in water for 6 h and then washed with ethanol and dried under room temperature. SERS spectra were obtained using a Horiba Jobin Yvon LabRAM HR spectrometer equipped with an integral microscope (Olympus BX 41). The 632.8 nm radiation from an air-cooled He/Ne laser was used as the excitation source. The laser beam (4.25 mW) was focused onto a spot (*ca.* 1 mm diameter) with an objective lens (50×, NA = 0.50). Data acquisition times were usually 15 s. The holographic grating (600 grooves/mm) and the slit allowed a spectral resolution of 1 cm^{-1}. The Raman band of a Si wafer at 520 cm^{-1} was used to calibrate the spectrometer. All SERS spectra were obtained by averaging more than five spectra recorded at different areas on the surface.

Conflict of Interest: The authors declare no competing financial interest.

Acknowledgment. This work was supported by Basic Science Research Programs (2010-0029149) and EPB Center (2008-0061892) through the NRF funded by the Korean government (MSIP) and was also supported by the Institute for Basic Science in Korea and the Industrial Core Technology Development Program by the Ministry of Trade, Industry & Energy (10037397).

Supporting Information Available: Additional experimental data (Figures S1–11). This material is available free of charge *via* the Internet at http://pubs.acs.org.

REFERENCES AND NOTES

1. Rycenga, M.; Cobley, C. M.; Zeng, J.; Li, W.; Moran, C. H.; Zhang, Q.; Qin, D.; Xia, Y. Controlling the Synthesis and Assembly of Silver Nanostructures for Plasmonic Applications. *Chem. Rev.* **2011**, *111*, 3669–3712.
2. Cortie, M. B.; McDonagh, A. M. Synthesis and Optical Properties of Hybrid and Alloy Plasmonic Nanoparticles. *Chem. Rev.* **2011**, *111*, 3713–3735.
3. Kim, M.; Lee, Y. W.; Kim, D.; Lee, S.; Ryoo, S.-R.; Min, D.-H.; Lee, S. B.; Han, S. W. Reshaping Nanocrystals for Tunable Plasmonic Substrates. *ACS Appl. Mater. Interfaces* **2012**, *4*, 5038–5043.
4. Sau, T. K.; Rogach, A. L.; Jäckel, F.; Klar, T. A.; Feldmann, J. Properties and Applications of Colloidal Nonspherical Noble Metal Nanoparticles. *Adv. Mater.* **2010**, *22*, 1805–1825.
5. Saha, K.; Agasti, S. S.; Kim, C.; Li, X.; Rotello, V. M. Gold Nanoparticles in Chemical and Biological Sensing. *Chem. Rev.* **2012**, *112*, 2739–2779.
6. Qian, X.; Li, J.; Nie, S. Stimuli-Responsive SERS Nanoparticles: Conformational Control of Plasmonic Coupling and Surface Raman Enhancement. *J. Am. Chem. Soc.* **2009**, *131*, 7540–7541.
7. Lu, W.; Singh, A. K.; Khan, S. A.; Senapati, D.; Yu, H.; Ray, P. C. Gold Nano-Popcorn-Based Targeted Diagnosis, Nanotherapy Treatment, and *in Situ* Monitoring of Photothermal Therapy Response of Prostate Cancer Cells Using Surface-Enhanced Raman Spectroscopy. *J. Am. Chem. Soc.* **2010**, *132*, 18103–18104.
8. Hong, J. W.; Lee, S.-U.; Lee, Y. W.; Han, S. W. Hexoctahedral Au Nanocrystal with High-Index Facets and Their Optical and Surface-Enhanced Raman Scattering Properties. *J. Am. Chem. Soc.* **2012**, *134*, 4565–4568.
9. Xu, X.-H. N.; Chen, J.; Jeffers, R. B.; Kyriacou, S. Direct Measurement of Sizes and Dynamics of Single Living Membrane Transporters Using Nanooptics. *Nano Lett.* **2002**, *2*, 175–182.
10. Jang, H.; Ryoo, S.-R.; Kostarelos, K.; Han, S. W.; Min, D.-H. The Effective Nuclear Delivery of Doxorubicin from Dextran-Coated Gold Nanoparticles Larger than Nuclear Pores. *Biomaterials* **2013**, *34*, 3503–3510.
11. Gross, E.; Liu, J. H.-C.; Toste, F. D.; Somorjai, G. A. Control of Selectivity in Heterogeneous Catalysis by Tuning Nanoparticle Properties and Reactor Residence Time. *Nat. Chem.* **2012**, *4*, 947–952.
12. Zhang, Y.; Cui, X.; Shi, F.; Deng, Y. Nano-Gold Catalysis in Fine Chemical Synthesis. *Chem. Rev.* **2012**, *112*, 2467–2505.
13. Toshima, N.; Yonezawa, T. Bimetallic Nanoparticles-Novel Materials for Chemical and Physical Applications. *New J. Chem.* **1998**, *22*, 1179–1201.
14. Kang, S. W.; Lee, Y. W.; Kim, M. J.; Hong, J. W.; Han, S. W. One-Pot Synthesis of Carbon-Supported Dendritic Pd-Au Nanoalloys for Electrocatalytic Ethanol Oxidation. *Chem. Asian J.* **2011**, *6*, 909–913.
15. Wang, L.; Nemoto, Y.; Yamauchi, Y. Direct Synthesis of Spatially-Controlled Pt-on-Pd Bimetallic Nanodendrites with Superior Electrocatalytic Activity. *J. Am. Chem. Soc.* **2011**, *133*, 9674–9677.
16. Xia, Y.; Xiong, Y.; Lim, B.; Skrabalak, S. E. Shape-Controlled Synthesis of Metal Nanocrystals: Simple Chemistry Meets Complex Physics?. *Angew. Chem., Int. Ed.* **2008**, *48*, 60–103.
17. Yin, A.-X.; Min, X.-Q.; Zhang, Y.-W.; Yan, C.-H. Shape-Selective Synthesis and Facet-Dependent Enhanced Electrocatalytic Activity and Durability of Monodisperse Sub-10 nm Pt-Pd Tetrahedrons and Cubes. *J. Am. Chem. Soc.* **2011**, *133*, 3816–3819.
18. Narayanan, R.; El-Sayed, M. A. Shape-Dependent Catalytic Activity of Platinum Nanoparticles in Colloidal Solution. *Nano Lett.* **2004**, *4*, 1343–1348.
19. Wu, J.; Gross, A.; Yang, H. Shape and Composition-Controlled Platinum Alloy Nanocrystals Using Carbon Monoxide as Reducing Agent. *Nano Lett.* **2011**, *11*, 798–802.
20. Hong, J. W.; Kim, D.; Lee, Y. W.; Kim, M.; Kang, S. W.; Han, S. W. Atomic-Distribution-Dependent Electrocatalytic Activity of Au–Pd Bimetallic Nanocrystals. *Angew. Chem., Int. Ed.* **2011**, *50*, 8876–8880.
21. Zhang, J.; Yang, H.; Fang, J.; Zou, S. Synthesis and Oxygen Reduction Activity of Shape-Controlled Pt$_3$Ni Nanopolyhedra. *Nano Lett.* **2010**, *10*, 638–644.
22. Lee, Y. W.; Kim, M.; Kang, S. W.; Han, S. W. Polyhedral Bimetallic Alloy Nanocrystals Exclusively Bound by {110} Facets: Au–Pd Rhombic Dodecahedra. *Angew. Chem., Int. Ed.* **2011**, *50*, 3466–3470.
23. Xue, C.; Millstone, J. E.; Li, S.; Mirkin, C. A. Plasmon-Driven Synthesis of Triangular Core–Shell Nanoprisms from Gold Seeds. *Angew. Chem., Int. Ed.* **2007**, *46*, 8436–8439.
24. Kim, M.; Lee, K. Y.; Jeong, G. H.; Jang, J.; Han, S. W. Fabrication of Au–Ag Alloy Nanoprisms with Enhanced Catalytic Activity. *Chem. Lett.* **2007**, *36*, 1350–1351.
25. Ma, Y.; Li, W.; Cho, E. C.; Li, Z.; Yu, T.; Zeng, J.; Xie, Z.; Xia, Y. Au@Ag Core–Shell Nanocubes with Finely Tuned and Well-Controlled Sizes, Shell Thicknesses, and Optical Properties. *ACS Nano* **2010**, *4*, 6725–6734.
26. Choi, S.-I.; Choi, R.; Han, S. W.; Park, J. T. Synthesis and Characterization of Pt$_9$Co Nanocubes with High Activity for Oxygen Reduction. *Chem. Commun.* **2010**, *46*, 4950–4952.
27. Choi, S.-I.; Choi, R.; Han, S. W.; Park, J. T. Shape-Controlled Synthesis of Pt$_3$Co Nanocrystals with High Electrocatalytic Activity toward Oxygen Reduction. *Chem.—Eur. J.* **2011**, *17*, 12280–12284.
28. Yuan, Q.; Zhou, Z.; Zhuang, J.; Wang, X. Seed Displacement, Epitaxial Synthesis of Rh/Pt Bimetallic Ultrathin Nanowires for Highly Selective Oxidizing Ethanol to CO$_2$. *Chem. Mater.* **2010**, *22*, 2395–2402.
29. Fischler, M.; Simon, U.; Nir, H.; Eichen, Y.; Burley, G. A.; Gierlich, J.; Gramlich, P. M. E.; Carell, T. Formation of Bimetallic Ag-Au Nanowires by Metallization of Artificial DNA Duplexes. *Small* **2007**, *3*, 1049–1055.
30. Xu, J.; Wilson, A. R.; Rathmell, A. R.; Howe, J.; Chi, M.; Wiley, B. J. Synthesis and Catalytic Properties of Au–Pd Nanoflowers. *ACS Nano* **2011**, *5*, 6119–6127.
31. Lee, Y. W.; Kim, N. H.; Lee, K. Y.; Kwon, K.; Kim, M.; Han, S. W. Synthesis and Characterization of Flower-Shaped Porous Au-Pd Alloy Nanoparticles. *J. Phys. Chem. C* **2008**, *112*, 6717–6722.
32. Lim, B.; Jiang, M.; Camargo, P. H. C.; Cho, E. C.; Tao, J.; Lu, X.; Zhu, Y.; Xia, Y. Pd-Pt Bimetallic Nanodendrites with High Activity for Oxygen Reduction. *Science* **2009**, *324*, 1302–1305.
33. Guo, S.; Li, J.; Dong, S.; Wang, E. Three-Dimensional Pt-On-Au Bimetallic Dendritic Nanoparticle: One-Step,

High-Yield Synthesis and Its Bifunctional Plasmonic and Catalytic Properties. *J. Phys. Chem. C* **2010**, *114*, 15337–15342.

34. Lee, Y. W.; Kim, M.; Kim, Y.; Kang, S. W.; Lee, J.-H.; Han, S. W. Synthesis and Electrocatalytic Activity of Au-Pd Alloy Nanodendrites for Ethanol Oxidation. *J. Phys. Chem. C* **2010**, *114*, 7689–7693.
35. Lu, C.-L.; Prasad, K. S.; Wu, H.-L.; Ho, J. A.; Huang, M. H. Au Nanocube-Directed Fabrication of Au-Pd Core-Shell Nanocrystals with Tetrahexahedral, Concave Octahedral, and Octahedral Structures and Their Electrocatalytic Activity. *J. Am. Chem. Soc.* **2010**, *132*, 14546–14553.
36. Kim, D.; Lee, Y. W.; Lee, S. B.; Han, S. W. Convex Polyhedral Au@Pd Core−Shell Nanocrystals with High-Index Facets. *Angew. Chem., Int. Ed.* **2012**, *51*, 159–163.
37. Lee, Y. W.; Kim, D.; Hong, J. W.; Kang, S. W.; Lee, S. B.; Han, S. W. Kinetically Controlled Growth of Polyhedral Bimetallic Alloy Nanocrystals Exclusively Bound by High-Index Facets: Au−Pd Hexoctahedra. *Small* **2013**, *9*, 660–665.
38. Hong, J. W.; Kim, M.; Kim, Y.; Han, S. W. Trisoctahedral Au−Pd Alloy Nanocrystals with High-Index Facets and Their Excellent Catalytic Performance. *Chem.—Eur. J.* **2012**, *18*, 16626–16630.
39. Zhang, L.; Zhang, J.; Kuang, Q.; Xie, S.; Jiang, Z.; Xie, Z.; Zheng, L. Cu^{2+}-Assisted Syntehsis of Hexoctahedral Au-Pd Alloy Nanocrystals with High-Index Facets. *J. Am. Chem. Soc.* **2011**, *133*, 17114–17117.
40. González, E.; Arbiol, J.; Puntes, V. F. Carving at the Nanoscale: Sequential Galvanic Exchange and Kirkendall Growth at Room Temperature. *Science* **2011**, *334*, 1377–1380.
41. Wang, L.; Yamauchi, Y. Autoprogrammed Synthesis of Triple-Layered Au@Pd@Pt Core−Shell Nanoparticles Consisting of a Au@Pd Bimetallic Core and Nanoporous Pt Shell. *J. Am. Chem. Soc.* **2010**, *132*, 13636–13638.
42. Wang, L.; Yamauchi, Y. Strategic Synthesis of Trimetallic Au@Pd@Pt Core-Shell Nanoparticles from Poly(vinylpyrrolidone)-Based Aqueous Solution toward Highly Active Electrocatalysts. *Chem. Mater.* **2011**, *23*, 2457–2465.
43. Choi, B.-S.; Lee, Y. W.; Kang, S. W.; Hong, J. W.; Kim, J.; Park, I.; Han, S. W. Multimetallic Alloy Nanotubes with Nanoporous Framework. *ACS Nano* **2012**, *6*, 5659–5667.
44. Wu, H.; Li, H.; Zhai, Y.; Xu, X.; Jin, Y. Facile Synthesis of Free-Standing Pd-Based Nanomembranes with Enhanced Catalytic Performance for Methanol/Ethanol Oxidation. *Adv. Mater.* **2012**, *24*, 1594–1597.
45. Hong, J. W.; Kang, S. W.; Choi, B.-S.; Kim, D.; Lee, S. B.; Han, S. W. Controlled Synthesis of Pd-Pt Alloy Hollow Nanostructures with Enhanced Catalytic Activities for Oxygen Reduction. *ACS Nano* **2012**, *6*, 2410–2419.
46. Lee, Y. W.; Kim, M.; Kim, Z. H.; Han, S. W. One-Step Synthesis of Au@Pd Core−Shell Nanooctahedron. *J. Am. Chem. Soc.* **2009**, *131*, 17036–17037.
47. Kim, Y.; Hong, J. W.; Lee, Y. W.; Kim, M.; Kim, D.; Yun, W. S.; Han, S. W. Synthesis of AuPt Heteronanostructures with Enhanced Electrocatalytic Activity toward Oxygen Reduction. *Angew. Chem., Int. Ed.* **2010**, *49*, 10197–10201.
48. Wang, D.; Li, Y. Bimetallic Nanocrystals: Liquid-Phase Synthesis and Catalytic Applications. *Adv. Mater.* **2011**, *23*, 1044–1060.
49. Ferrando, R.; Jellinek, J.; Johnston, R. L. Nanoalloy: From Theory to Application of Alloy Clusters and Nanoparticles. *Chem. Rev.* **2008**, *108*, 845–910.
50. Tao, A. R.; Habas, S.; Yang, P. Shape Control of Colloidal Metal Nanocrystals. *Small* **2008**, *4*, 310–325.
51. Lee, K. Y.; Kim, M.; Lee, Y. W.; Lee, J.-J.; Han, S. W. Fabrication of Metal Nanoparticles-Carbon Nanotubes Composite Materials in Solution. *Chem. Phys. Lett.* **2007**, *440*, 249–252.
52. Fu, R.; Zeng, H.; Lu, Y.; Lai, S. Y.; Chan, W. H.; Ng, C. F. The Reduction of Pt(IV) with Activated Carbon Fibers-An XPS Study. *Carbon* **1995**, *33*, 657–661.
53. Heo, J.; Kim, D.-S.; Kim, Z. H.; Lee, Y. W.; Kim, D.; Kim, M.; Kwon, K.; Park, H. J.; Yun, W. S.; Han, S. W. Controlled Synthesis and Characterization of the Enhanced Local Field of Octahedral Au Nanocrystals. *Chem. Commun.* **2008**, 6120–6122.
54. Zhang, J.; Zhang, L.; Xie, S.; Kuang, Q.; Han, X.; Xie, Z.; Zheng, L. Synthesis of Concave Palladium Nanocubes with High-Index Surfaces and High Electrocatalytic Activities. *Chem.—Eur. J.* **2011**, *17*, 9915–9919.
55. Berhault, G.; Bausach, M.; Bisson, L.; Becerra, L.; Thomazeau, C.; Uzio, D. Seed-Mediated Synthesis of Pd Nanocrystals: Factors Influencing a Kinetic- or Thermodynamic-Controlled Growth Regime. *J. Phys. Chem. C* **2007**, *111*, 5915–5925.
56. Niu, Z.; Peng, Q.; Gong, M.; Rong, H.; Li, Y. Oleylamine-Mediated Shape Evolution of Palladium Nanocrystals. *Angew. Chem., Int. Ed.* **2011**, *50*, 6315–6319.
57. DeSantis, C. J.; Peverly, A. A.; Peters, D. G.; Skrabalak, S. E. Octopods versus Concave Nanocrystals: Control of Morphology by Manipulating the Kinetics of Seeded Growth *via* Co-Reduction. *Nano Lett.* **2011**, *11*, 2164–2168.
58. Grote, M.; Hüppe, U.; Kettrup, A. Solvent Extraction of Noble Metals by Formazans-I Comparative Study on the Extractability of Pt(IV), Pd(II) and Ag(I) by Formazans Combined with a Liquid Anion-Exchanger. *Talanta* **1984**, *31*, 755–762.
59. D'Souza, L.; Sampath, S. Preparation and Characterization of Silane-Stabilized, Highly Uniform, Nanobimetallic Pt-Pd Particles in Solid and Liquid Matrixes. *Langmuir* **2000**, *16*, 8510–8517.
60. Lee, H.; Habas, S. E.; Somorjai, G. A.; Yang, P. Localized Pd Overgrowth on Cubic Pt Nanocrystals for Enhanced Electrocatalytic Oxidation of Formic Acid. *J. Am. Chem. Soc.* **2008**, *130*, 5406–5407.
61. Zhang, H.; Jin, M.; Xia, Y. Enhancing the Catalytic and Electrocatalytic Properties of Pt-Based Catalysts by Forming Bimetallic Nanocrystals with Pd. *Chem. Soc. Rev.* **2012**, *41*, 8035–8049.
62. Wang, L.; Yamauchi, Y. Synthesis of Mesoporous Pt Nanoparticles with Uniform Particle Size from Aqueous Surfactant Solutions toward Highly Active Electrocatalysts. *Chem.—Eur. J.* **2011**, *17*, 8810–8815.
63. Strasser, P.; Koh, S.; Anniyev, T.; Greeley, J.; More, K.; Yu, C.; Liu, Z.; Kaya, S.; Nordlund, D.; Ogasawara, H.; Toney, M. F.; Nilsson, A. Lattice-Strain Control of the Activity in Dealloyed Core-Shell Fuel Cell Catalysts. *Nat. Chem.* **2010**, *2*, 454–460.
64. Tang, W.; Henkelman, G. Charge Redistribution in Core-Shell Nanoparticles to Promote Oxygen Reduction. *J. Chem. Phys.* **2009**, *130*, 194504.
65. Hammer, B.; Morikawa, Y.; Nørskov, J. K. CO Chemisorption at Metal Surfaces and Overlayers. *Phys. Rev. Lett.* **1996**, *76*, 2141–2144.
66. Choi, R.; Choi, S.-I.; Choi, C. H.; Nam, K. M.; Woo, S. I.; Park, J. T.; Han, S. W. Designed Synthesis of Well-Defined Pd@Pt Core-Shell Nanoparticles with Controlled Shell Thickness as Efficient Oxygen Reduction Electrocatalysts. *Chem.—Eur. J.* **2013**, *19*, 8190–8198.
67. Ruban, A.; Hammer, B.; Stoltze, P.; Skriver, H. L.; Nørskov, J. K. Surface Electronic Structure and Reactivity of Transition and Noble Metals. *J. Mol. Catal. A: Chem.* **1997**, *115*, 421–429.
68. Hammer, B.; Nørskov, J. K. Theoretical Surface Science and Catalysis-Calculations and Concepts. *Adv. Catal.* **2000**, *45*, 71–129.
69. Nilsson, A.; Pettersson, L. G. M.; Hammer, B.; Bligaard, T.; Christensen, C. H.; Nørskov, J. K. The Electronic Structure Effect in Heterogeneous Catalysis. *Catal. Lett.* **2005**, *100*, 111–114.
70. Choi, S.-I.; Lee, S.-U.; Kim, W. Y.; Choi, R.; Hong, K.; Nam, K. M.; Han, S. W.; Park, J. T. Composition-Controlled PtCo Alloy Nanocubes with Tuned Electrocatalytic Activity for Oxygen Reduction. *ACS Appl. Mater. Interfaces* **2012**, *4*, 6228–6234.
71. Park, K.-H.; Lee, Y. W.; Kim, Y.; Kang, S. W.; Han, S. W. One-Pot Synthesis of CeO_2-Supported Pd-Cu Alloy Nanocubes with High Catalytic Activity. *Chem.—Eur. J.* **2013**, *19*, 8053–8057.
72. Kuo, C.-H.; Yang, Y.-C.; Gwo, S.; Huang, M. H. Facet-Dependent and Au Nanocrystal-Enhanced Electrical and Photocatalytic

Properties of Au-Cu_2O Core-Shell Heterostructures. *J. Am. Chem. Soc.* **2011**, *133*, 1052–1057.

73. Kim, K.; Lee, S. J.; Kim, K. L. Surface-Enhanced Raman Scattering of 4-Nitrothioanisole in Ag Sol. *J. Phys. Chem. B* **2004**, *108*, 16208–16212.
74. Tian, Z.-Q.; Ren, B.; Li, J.-F.; Yang, Z.-L. Expanding Generality of Surface-Enhanced Raman Spectroscopy with Borrowing SERS Activity Strategy. *Chem. Commun.* **2007**, *34*, 3514–3534.
75. Abdelsalam, M. E.; Mahajan, S.; Bartlett, P. N.; Baumberg, J. J.; Russell, A. E. SERS at Structured Palladium and Platinum Surfaces. *J. Am. Chem. Soc.* **2007**, *129*, 7399–7406.
76. Zhang, K.; Xiang, Y.; Wu, X.; Feng, L.; He, W.; Liu, J.; Zhou, W.; Xie, S. Enhanced Optical Responses of Au@Pd Core/Shell Nanobars. *Langmuir* **2009**, *25*, 1162–1168.
77. Kan, C.; Cai, W.; Li, C.; Zhang, L.; Hofmeister, H. Ultrasonic Synthesis and Optical Properties of Au/Pd Bimetallic Nanoparticles in Ethylene Glycol. *J. Phys. D: Appl. Phys.* **2003**, *36*, 1609–1614.
78. Park, W.-H.; Kim, Z. H. Charge Transfer Enhancement in the SERS of a Single Molecule. *Nano Lett.* **2010**, *10*, 4040–4048.
79. Bae, Y.; Kim, N. H.; Kim, M.; Lee, K. Y.; Han, S. W. Anisotropic Assembly of Ag Nanoprisms. *J. Am. Chem. Soc.* **2008**, *130*, 5432–5433.
80. Osawa, M.; Matsuda, N.; Yoshii, K.; Uchida, I. Charge Transfer Resonance Raman Process in Surface-Enhanced Raman Scattering from p-Aminothiophenol Adsorbed on Silver: Herzberg-Teller Contribution. *J. Phys. Chem.* **1994**, *98*, 12702–12707.
81. Xie, W.; Walkenfort, B.; Schlücker, S. Label-Free SERS Monitoring of Chemical Reactions Catalyzed by Small Gold Nanoparticles Using 3D Plasmonic Superstructures. *J. Am. Chem. Soc.* **2013**, *135*, 1657–1660.
82. Huang, J.; Zhu, Y.; Lin, M.; Wang, Q.; Zhao, L.; Yang, Y.; Yao, K. X.; Han, Y. Site-Specific Growth of Au−Pd Alloy Horns on Au Nanorods: A Platform for Highly Sensitive Monitoring of Catalytic Reactions by Surface Enhancement Raman Spectroscopy. *J. Am. Chem. Soc.* **2013**, *135*, 8552–8561.
83. Woods, R. In *Electroanalytical Chemistry: A Series of Advances*; Bard, A. J., Eds.; Marcel Dekker: New York, 1974; Vol. 9, pp 1−162.